A&A 551, A137 (2013)
DOI: 10.1051/0004-6361/201219568

Astronomy & Astrophysics

Phase relations for seismology of photospheric flux tubes

M. G. Moreels and T. Van Doorsselaere⋆

Centre for mathematical Plasma Astrophysics, Mathematics Department, KU Leuven, Celestijnenlaan 200B bus 2400, 3001 Leuven, Belgium
e-mail: michael.moreels@wis.kuleuven.be

Received 9 May 2012 / Accepted 22 January 2013

ABSTRACT

Aims. We present a mathematical framework for the seismology of photospheric flux tubes using a uniform straight cylinder as a flux-tube model. In contrast to the earlier model of Fujimura & Tsuneta (2009, ApJ, 702, 1443), we also include a non-zero gas pressure; we do not use the thin tube approximation and we use an underdense region inside the flux tube.
Methods. We used the linearised ideal magnetohydrodynamic equations to describe different wave modes in the photosphere. Using the wave mode polarisations we then obtained phase relations which represent different observables. Those phase relations were used to calculate phase differences and amplitude ratios. Finally we inverted these amplitude ratios to obtain plasma parameters which are not directly observable.
Results. The mathematical framework results in phase differences that can be conveniently compared with observational data to distinguish between different wave modes. Once the wave mode has been identified, the inverted amplitude ratios can be used to either analytically or numerically estimate the magnitude of plasma parameters which are not directly observable, such as the vertical wavenumber. Artificial observations of different wave modes have shown that the framework mostly succeeds in identifying the correct wave mode and in reproducing the correct plasma parameters using the inverted amplitude ratios.

Key words. Magnetohydrodynamics (MHD) – methods: analytical – Sun: photosphere – Sun: oscillations

1. Introduction

Since the discovery of solar oscillations in 1960 (Leighton 1960), there have been numerous observations of wave motions in the solar atmosphere (Stein & Leibacher 1974). Recently, modern ground- and space-based observational instruments show ubiquitous waves in different parts of the solar atmosphere. They were detected in the corona using the Extreme ultraviolet Imaging Telescope (EIT) aboard the Solar and Heliospheric Observatory (SOHO; Thompson et al. 1999); they were also detected with the imaging telescope on board the Transition Region and Coronal Explorer (TRACE) spacecraft (Nakariakov et al. 1999). More recently, such magnetohydrodynamic (MHD) waves were observed in the corona with the Coronal Multi-Channel Polarimeter (CoMP; Tomczyk et al. 2007), with the extreme ultraviolet imaging spectrometer (EIS) aboard Hinode (Van Doorsselaere et al. 2008; Banerjee et al. 2009), and with the Solar Dynamics Observatory Atmospheric Imaging Assembly (SDO/AIA; Liu et al. 2010; Morton et al. 2012). Magnetohydrodynamic waves are also found in the chromosphere using the Solar Optical Telescope (SOT) aboard Hinode (De Pontieu et al. 2007) and using the Swedish Solar Telescope (SST; Jess et al. 2009).

These observations of MHD waves can be used to do seismology. This is a technique to find local physical quantities of the plasma which are not directly observable by matching MHD theory of waves with observations (Uchida 1970). This technique has been applied successfully in the corona where it is termed coronal seismology (Nakariakov & Verwichte 2005) and has been successful in determining the coronal magnetic field strength (Nakariakov et al. 1999), the transverse structuring of the flux tubes (Aschwanden et al. 2003; Goossens et al. 2008), the coronal density stratification (Andries et al. 2005), the adiabatic index and thermal conduction (Van Doorsselaere et al. 2011b), and the flare plasma β (Van Doorsselaere et al. 2011a).

Recently MHD waves have also been observed in photospheric flux tubes using SOT (Fujimura & Tsuneta 2009) and using the Rapid Oscillations in the Solar Atmosphere imaging system (ROSA; Morton et al. 2011; Jess et al. 2012a,b). Fujimura & Tsuneta (2009) have made the first step towards photospheric seismology; they reported observations of oscillations in photospheric flux tubes and used those observations to find local physical quantities of the plasma, such as the density. We would like to point out that photospheric seismology differs from helioseismology (Ulrich 1970; Deubner 1983) in the sense that helioseismology studies global waves of the sun to derive average physical quantities, while photospheric seismology focusses on local waves to derive local physical quantities. Photospheric seismology is complementary to local helioseismology (Gizon & Birch 2005): local helioseismology focusses more on inward/outward traveling waves around sunspots or magnetic pores, while photospheric seismology studies waves that are confined to the magnetic structures.

In this article we construct a theoretical framework in order to do photospheric seismology. The aim of this article is to improve upon the modelling done in Fujimura & Tsuneta (2009) first, by including a non-zero gas pressure in the equilibrium model; second, by not using the thin tube approximation in our model; and third, by using an underdense pore instead of an overdense pore. This model is thus an improvement for the modelling of photospheric flux tubes, but some important physical effects (e.g. density stratification) are still omitted in the equilibrium model. We will calculate the phase diagram of wave modes in

⋆ Postdoctoral fellow of the FWO-Vlaanderen.

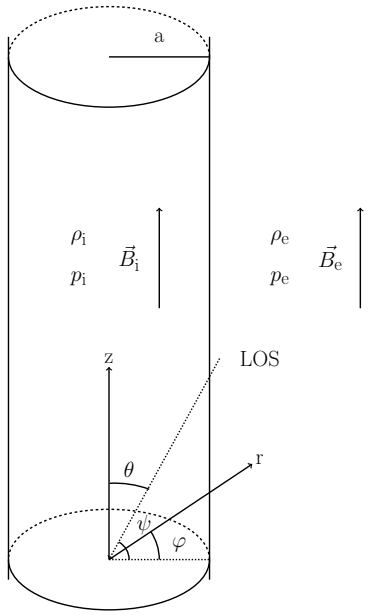

Fig. 1. Equilibrium configuration of the flux tube combined with the line of sight (LOS). The LOS angle θ is the angle between the LOS and the z-axis. The LOS angle ψ is the angle between the LOS and the $\varphi = 0$ axis.

the photosphere and calculate their polarisations. Then we will derive the phase relations between different observable quantities such as the line of sight (LOS) velocity perturbation, the LOS magnetic field perturbation, and the intensity perturbation. Using those phase relations we can derive phase differences and amplitude ratios between the observable quantities. The phase differences can be used to distinguish between different wave modes, while the amplitude ratios will be inverted to obtain information on physical parameters that are not directly observable. We will use artificial observations to check the validity of the theoretical framework.

2. Mathematical framework

We model a flux tube as a straight cylinder with a constant radius R. The plasma is uniform both inside and outside the cylinder with a possible jump at the boundary (cf. Edwin & Roberts 1983). The magnetic field is directed along the axis of the flux tube and is given by $B_{0,\mathrm{i}}$ inside the flux tube and $B_{0,\mathrm{e}}$ outside the flux tube. The plasma pressure and density are $p_{0,\mathrm{i}}$ and $\rho_{0,\mathrm{i}}$ inside the flux tube and outside the flux tube they are $p_{0,\mathrm{e}}$ and $\rho_{0,\mathrm{e}}$. We assume that the plasma has no background flow, i.e. the equilibrium velocity is $v_0 = 0$ both inside and outside the flux tube. A sketch of the equilibrium is shown in Fig. 1. We want to point out that this model takes one more step (compared to Fujimura & Tsuneta 2009) in modelling photospheric flux tubes. First, we included a non-zero gas pressure in the equilibrium model; second, we did not use the thin tube approximation in our model; third, we used an underdense region inside the flux tube instead of an overdense region. We also want to point out that this model omits important physics, e.g. density stratification (Osterbrock 1961; Rosenthal et al. 2002; Erdélyi et al. 2007), but the idea is to use a very simple model to illustrate the possibility of photospheric seismology.

2.1. Dispersion diagram

The ideal MHD equations can be linearised around the equilibrium state and are given by

$$\frac{\partial \rho'}{\partial t} = -\rho_0 \Delta \tag{1}$$

$$\rho_0 \frac{\partial \boldsymbol{v}'}{\partial t} = -\nabla p' + \frac{1}{\mu}(\nabla \times \boldsymbol{B}') \times \boldsymbol{B}_0 \tag{2}$$

$$\frac{\partial \boldsymbol{B}'}{\partial t} = -\boldsymbol{B}_0 \Delta + (\boldsymbol{B}_0 \cdot \nabla)\boldsymbol{v}' \tag{3}$$

$$\frac{\partial p'}{\partial t} = -\gamma p_0 \Delta, \tag{4}$$

where

$$\Delta = \nabla \cdot \boldsymbol{v}'.$$

These equations are valid everywhere. In these equations the subscript 0 indicates equilibrium quantities and the perturbed quantities are denoted with a prime. The constant γ is the ratio of specific heats and the constant μ is the magnetic permeability. The above equations can be solved analytically (cf. Edwin & Roberts 1983) by performing a Fourier analysis in the ignorable coordinates. Thus, the compression inside the flux tube can be written as $\Delta = \omega R(r) \exp[\mathrm{i}(\omega t + m\varphi + kz)]$, the multiplication by ω is to ensure the correct dimensions. The main results are the dispersion relations of the different wave modes in the photosphere. For surface modes (i.e. $\kappa_\mathrm{i}^2 > 0$) we get

$$\rho_{0,\mathrm{i}}\left(k^2 c_{\mathrm{A,i}}^2 - \omega^2\right)\kappa_\mathrm{e}\frac{K_m'(\kappa_\mathrm{e}R)}{K_m(\kappa_\mathrm{e}R)} = \rho_{0,\mathrm{e}}\left(k^2 c_{\mathrm{A,e}}^2 - \omega^2\right)\kappa_\mathrm{i}\frac{I_m'(\kappa_\mathrm{i}R)}{I_m(\kappa_\mathrm{i}R)} \tag{5}$$

and for body modes (i.e. $\kappa_\mathrm{i}^2 = -n_\mathrm{i}^2 < 0$) we get

$$\rho_{0,\mathrm{i}}\left(k^2 c_{\mathrm{A,i}}^2 - \omega^2\right)\kappa_\mathrm{e}\frac{K_m'(\kappa_\mathrm{e}R)}{K_m(\kappa_\mathrm{e}R)} = \rho_{0,\mathrm{e}}\left(k^2 c_{\mathrm{A,e}}^2 - \omega^2\right)n_\mathrm{i}\frac{J_m'(n_\mathrm{i}R)}{J_m(n_\mathrm{i}R)}, \tag{6}$$

where the dash denotes the derivative of a Bessel function (e.g. $I_m'(\kappa_\mathrm{i}R) = (\mathrm{d}/\mathrm{d}x)I_m(x)$ evaluated at $x = \kappa_\mathrm{i}R$). We also have

$$\kappa^2 = \frac{\left(k^2 c_\mathrm{s}^2 - \omega^2\right)\left(k^2 c_\mathrm{A}^2 - \omega^2\right)}{\left(c_\mathrm{s}^2 + c_\mathrm{A}^2\right)\left(k^2 c_\mathrm{T}^2 - \omega^2\right)}$$

with the tube speed defined as

$$c_\mathrm{T} = \frac{c_\mathrm{s} c_\mathrm{A}}{\left(c_\mathrm{s}^2 + c_\mathrm{A}^2\right)^{1/2}}$$

and where $c_\mathrm{s} = (\gamma p_0/\rho_0)^{1/2}$ and $c_\mathrm{A} = B_0/(\mu\rho_0)^{1/2}$ are the sound and Alfvén speeds.

We can solve these dispersion relations numerically; here we use the same values for the sound and Alfvén speeds as Edwin & Roberts (1983) used for the photosphere, namely $c_{\mathrm{A,i}} = 2\,c_{\mathrm{s,i}}$, $c_{\mathrm{A,e}} = 0.5\,c_{\mathrm{s,i}}$, and $c_{\mathrm{s,e}} = 1.5\,c_{\mathrm{s,i}}$. We only looked at the sausage ($m = 0$) and the kink ($m = 1$) modes; the results are displayed in Fig. 2. In the figure the kink speed c_k is used which is given by

$$c_\mathrm{k} = \left(\frac{\rho_{0,\mathrm{i}} c_{\mathrm{A,i}}^2 + \rho_{0,\mathrm{e}} c_{\mathrm{A,e}}^2}{\rho_{0,\mathrm{i}} + \rho_{0,\mathrm{e}}}\right)^{1/2}.$$

The equivalent figure for coronal circumstances is well known. The current figure is less used. Different wave modes can be distinguished. Starting at the top we have the fast modes with

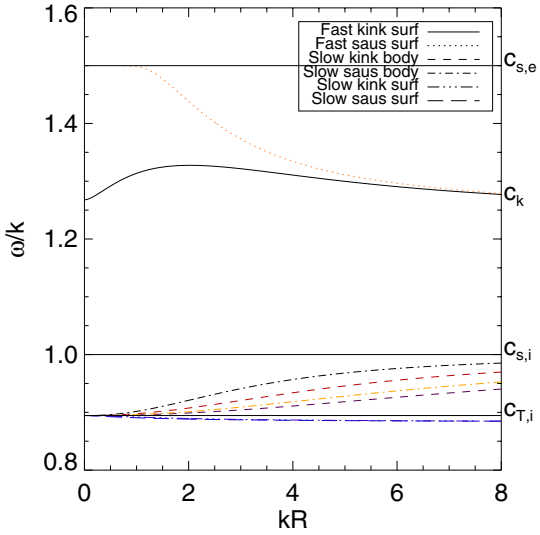

Fig. 2. Phase speed diagram of wave modes under photospheric conditions. We have taken $c_{\mathrm{A,i}} = 2\,c_{\mathrm{s,i}}$, $c_{\mathrm{A,e}} = 0.5\,c_{\mathrm{s,i}}$, and $c_{\mathrm{s,e}} = 1.5\,c_{\mathrm{s,i}}$. The Alfvén speeds are not indicated on the graph because no modes with real frequencies appear in that vicinity. The modes with phase speeds between $c_{\mathrm{T,i}}$ and $c_{\mathrm{s,i}}$ are body modes and the other modes are surface modes. Note that we only plotted four body modes, while there are actually infinitely many.

phase speeds above the internal sound speed $c_{\mathrm{s,i}}$; these are surface modes and we plotted only the $m = 0$ and $m = 1$ modes. Firstly, we would like to point out that these modes are actually surface Alfvén waves (Goossens et al. 2012) and that the terminology "fast modes" is used here to indicate that the modes have phase speeds above the internal sound speed $c_{\mathrm{s,i}}$. Secondly, it may look like the sausage surface mode has a cut-off at the external sound speed $c_{\mathrm{s,e}}$, but we suspect this is due to a lack of numerical resolution. For modes with $m > 1$, the phase speeds are lower than the phase speed of the kink mode but still above the kink speed c_{k}. "Slow modes" have phase speeds below the internal sound speed and can be split in either body or surface modes. The slow body modes have phase speeds between the internal sound speed $c_{\mathrm{s,i}}$ and the internal tube speed $c_{\mathrm{T,i}}$, while the slow surface modes have phase speeds below the internal tube speed. For the slow surface modes we plotted only the $m = 0$ and $m = 1$ modes, which have practically identical phase speeds with no cut-off frequency; higher values of m are very similar. We plotted four slow body modes which are the fundamental and first radial overtone of the $m = 0$ and $m = 1$ modes. Here, fundamental refers to the fact that they have the lowest number of nodes possible in the eigenfunction of ξ_r inside the flux tube (see Sect. 2.2 for more on eigenfunctions). Here, this means that the fundamental slow body modes have one node in the eigenfunctions inside the flux tube. When looking at radial overtones (i.e. more nodes inside the flux tube), the phase speed of the slow body modes decreases. Note that there are also infinitely many radial overtones. The phase speed also decreases for higher values of m.

2.2. Wave polarisation

Now we look at the polarisation of the wave modes. This can be done by calculating the displacement of the plasma $\boldsymbol{\xi}$. Equations (1)–(4) have been written and solved in terms of the compression Δ. Now we will solve those same equations in terms of the r-component of the displacement ξ_r and the total pressure perturbation P'. The solutions are

$$D\frac{\mathrm{d}}{\mathrm{d}r}(r\xi_r) = -CrP' \tag{7}$$

$$\frac{\mathrm{d}P'}{\mathrm{d}r} = \rho_0\left(\omega^2 - k^2c_{\mathrm{A}}^2\right)\xi_r, \tag{8}$$

where

$$D = \rho_0\left(c_{\mathrm{s}}^2 + c_{\mathrm{A}}^2\right)\left(\omega^2 - k^2c_{\mathrm{A}}^2\right)\left(\omega^2 - k^2c_{\mathrm{T}}^2\right)$$

and

$$C = \omega^4 - \left(c_{\mathrm{s}}^2 + c_{\mathrm{A}}^2\right)\left(\frac{m^2}{r^2} + k^2\right)\left(\omega^2 - k^2c_{\mathrm{T}}^2\right).$$

These equations match the equations in Sakurai et al. (1991), where B_φ is taken to be zero. The displacement of the plasma $\boldsymbol{\xi}$ also has a φ- and a z-component which are given by

$$\rho_0\left(\omega^2 - k^2c_{\mathrm{A}}^2\right)\xi_\varphi = \mathrm{i}\frac{m}{r}P' \tag{9}$$

$$\rho_0\left(\omega^2 - k^2c_{\mathrm{A}}^2\right)\xi_z = \mathrm{i}kP' + \mathrm{i}k\frac{B_0^2}{\mu}\nabla\cdot\boldsymbol{\xi}, \tag{10}$$

where

$$\nabla\cdot\boldsymbol{\xi} = \frac{-\omega^2P'}{\rho_0\left(c_{\mathrm{s}}^2 + c_{\mathrm{A}}^2\right)\left(\omega^2 - k^2c_{\mathrm{T}}^2\right)} = -\mathrm{i}R. \tag{11}$$

The above equations are valid both inside and outside the flux tube. Note that Eq. (9) shows that the sausage mode ($m = 0$) has no φ-component in the displacement.

Using Eqs. (7) and (8) we can now numerically calculate the eigenfunctions ξ_r and P' for different wave modes in the photosphere. Figure 3 shows the eigenfunctions for different sausage modes, normalised to their value at $r = R$. At the top of the figure we have the eigenfunction ξ_r and we note that indeed the eigenfunction confirms the distinction between the body and surface wave modes. The surface modes are largest near the surface of the flux tube ($r/R \approx 1$) but are evanescent away from the surface. The body mode on the other hand is largest inside the flux tube, meaning that the entire body of the flux tube moves. Also note that all modes are evanescent outside the flux tube, confirming that there is no propagation of energy away from the flux tube (i.e. we are not dealing with leaky modes). From the eigenfunction P' we again note the distinction between the surface and body modes, although the fast surface mode is also quite large inside the flux tube. This plot also shows that the fundamental body mode has one node inside the flux tube. This is contrary to what happens in coronal conditions where the fundamental mode has no nodes inside the flux tube.

Figure 4 shows the eigenfunctions for different kink modes. As in the case of sausage modes, all modes are evanescent outside the flux tube. As was the case with the eigenfunctions P' for the sausage modes, it could be argued that the fast surface mode is actually a body mode since the displacement inside the flux tube is quite large. Also, the slow body mode has a node in the fundamental radial mode which is not present under coronal conditions. The eigenfunctions P' do distinguish clearly between surface and body modes, and again we have the node inside the flux tube for the slow body mode.

Using Eqs. (7)–(10) we can calculate if a wave is mainly polarised longitudinally or transversely. The magnitude of the longitudinal displacement $\xi_\parallel$ is given by $\xi_\parallel = |\xi_z|$ and the magnitude

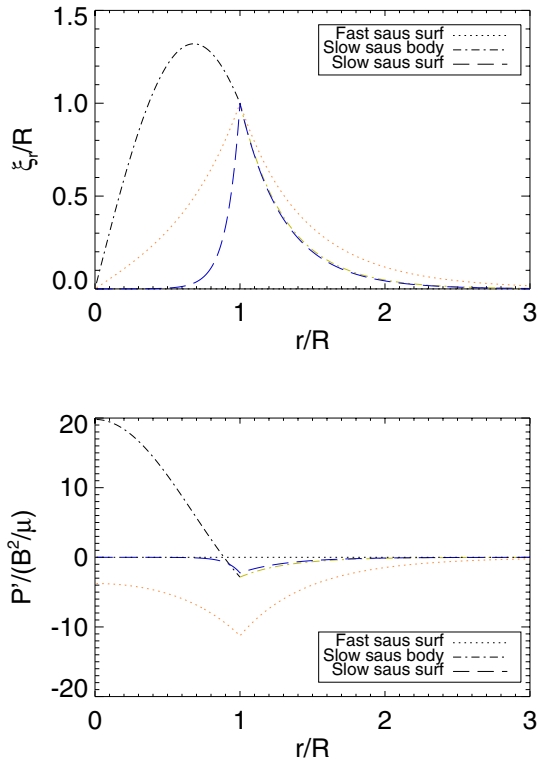

Fig. 3. Radial dependence of the eigenfunctions ξ_r and P' for sausage modes. We used the value $kR = 4$ and other physical parameters as in Fig. 2.

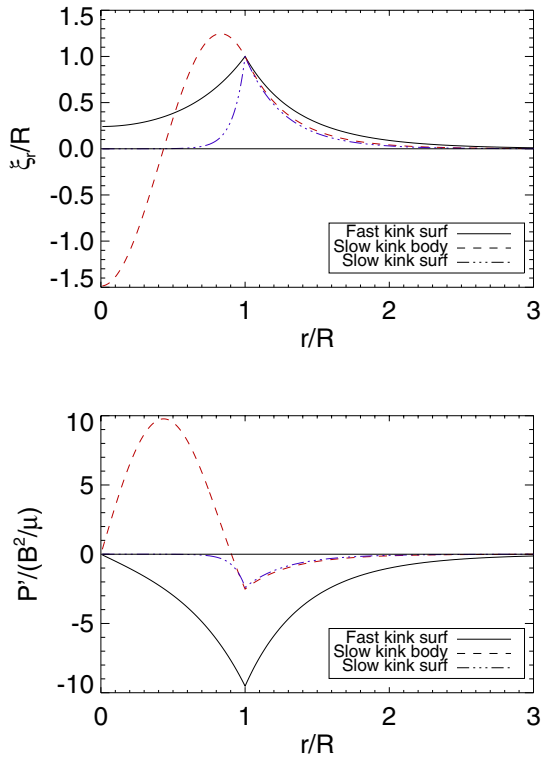

Fig. 4. Radial dependence of the eigenfunctions ξ_r and P' for kink modes. We used the value $kR = 4$ and other physical parameters as in Fig. 2.

of the transverse displacement $\xi_\perp$ is given by $\xi_\perp = \sqrt{|\xi_r|^2 + |\xi_\varphi|^2}$. We numerically calculated these magnitudes for different wave modes at the flux-tube boundary. The results are shown in Fig. 5. Note that the slow modes are dominated by the longitudinal component $\xi_\parallel$, this will be used in Sect. 2.3 to neglect the transverse components in seismology of slow modes. In fast modes the distinction is not clear cut. The fast sausage mode has $\xi_\parallel/\xi_\perp$ approximately 1 for all values kR. The fast kink mode is dominated by the transverse component $\xi_\perp$ for small kR, while for larger values of kR we again find that $\xi_\parallel/\xi_\perp$ is approximately 1. This means that fast modes have no dominant polarisation and we can neglect neither longitudinal nor transverse contributions to calculate the phase relations.

2.3. Phase relations

We can now calculate phase relations between different observable quantities using MHD theory. We start from Eqs. (1)–(4) and instead of performing a Fourier analysis of certain quantities, we prescribe Δ_i. We will focus on the inside of the flux tube since this part of the flux tube is the one mainly observed. We will discuss two cases, a propagating mode and a standing mode. For the propagating mode we say that $\Delta_i = \omega R_i(r) \sin(\omega t - kz + \alpha_z) \cos(m(\varphi - \alpha_\varphi))$, and for the standing mode we have $\Delta_i = \omega R_i(r) \sin(\omega t) \sin(kz + \alpha_z) \cos(m(\varphi - \alpha_\varphi))$. The phase shift α_z is determined by the height at which we observe the flux tube. It would not be possible to observe this phase shift, unless we had observations of the same wave at different heights (Jess et al. 2012a). The phase shift α_φ is determined by the LOS angle ψ which is the angle between the LOS and the axis $\varphi = 0$ (see Fig. 1). Later we will show that only sausage modes (i.e. $m = 0$) need to be studied and that the entire φ-dependence is uniform, thus we will drop the phase angle α_φ. From now on we will also drop the index i from the quantities since the observations only focus on the internal part of the flux tube. Equations (1)–(4) express the density, the pressure, the velocity, and the magnetic field perturbations in terms of the divergence of the velocity Δ described by the given expression.

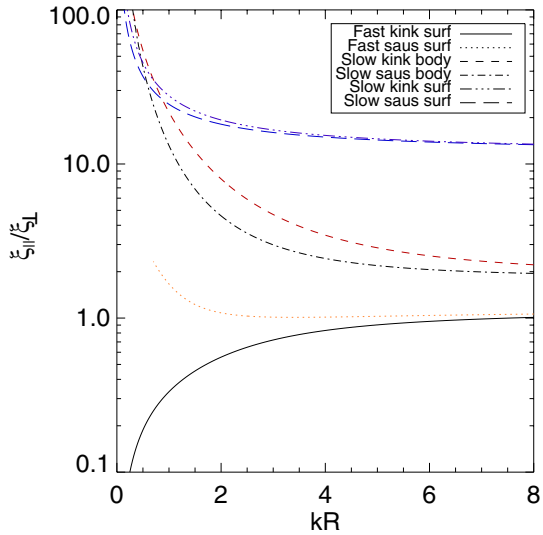

Fig. 5. Magnitude of the longitudinal displacement $\xi_\parallel$ divided by the magnitude of the transverse displacement $\xi_\perp$ at the flux-tube boundary as a function of kR for the different wave modes in the photosphere.

Typical observations this model could be applied to can be seen in Fujimura & Tsuneta (2009) and measure the intensity, the LOS velocity, and the LOS magnetic flux fluctuations. Since we know the theoretical expressions for the r-, φ-, and z-components of the velocity and the magnetic field perturbations, we can calculate the LOS velocity and the LOS magnetic

field perturbations. All we need is a way to calculate the intensity perturbation. By linearising the MHD equations we have expressed the density ρ as a sum of a constant background ρ_0 and a perturbation ρ', i.e. $\rho = \rho_0 + \rho'$, where the perturbation is small compared to the background (i.e. $\rho'/\rho_0 \ll 1$). Using the fact that the photosphere is optically thick and by assuming local thermodynamic equilibrium, we find that the continuum intensity is given by (e.g. Rutten 2003)

$$I = \frac{2h\nu^3}{c^2} \frac{1}{\exp(h\nu/k_\mathrm{B}T) - 1}, \tag{12}$$

where h is the Planck constant, k_B is the Boltzmann constant, T is the temperature of the plasma, ν is the frequency, and c is the speed of light. Using the values in Fujimura & Tsuneta (2009) for the temperature and the wavelength of the observations, we find that $h\nu/k_\mathrm{B}T \gtrsim 2$, which means we can approximate the intensity by

$$I \approx \frac{2h\nu^3}{c^2} \exp\left(-\frac{h\nu}{k_\mathrm{B}T}\right).$$

Modelling the plasma as an ideal gas ($T = \frac{\bar{\mu}p}{\bar{R}\rho}$ with $\bar{\mu}, \bar{R}$ constant) which undergoes adiabatic expansions/contractions ($p\rho^{-\gamma} = C$ with C constant), we find that the intensity I is approximated by

$$I \approx \frac{2h\nu^3}{c^2} \exp\left(-\frac{h\nu\bar{R}}{k_\mathrm{B}\bar{\mu}C}\rho^{-2/3}\right)$$

where we have used $\gamma = 5/3$. We can approximate $\rho^{-2/3}$ using $\rho = \rho_0 + \rho'$ to find $\rho^{-2/3} \approx \rho_0^{-2/3} - 2/3\rho_0^{-5/3}\rho'$. Substituting in the previous equation leads to

$$I \approx \frac{2h\nu^3}{c^2} \exp\left(-\frac{h\nu}{k_\mathrm{B}T_0}\right) \exp\left(\frac{2}{3}\frac{h\nu}{k_\mathrm{B}T_0}\frac{\rho'}{\rho_0}\right)$$

where we used $C \approx p_0\rho_0^{-5/3}$ and $T_0 = \frac{\bar{\mu}p_0}{\bar{R}\rho_0}$. Since $\rho' \ll \rho_0$, we can again approximate this by

$$I = I_0 + \frac{2}{3}\frac{h\nu}{k_\mathrm{B}T_0} I_0 \frac{\rho'}{\rho_0}, \tag{13}$$

where I_0 is given by

$$I_0 = 2\frac{h\nu^3}{c^2} \exp\left(-\frac{h\nu}{k_\mathrm{B}T_0}\right).$$

We will drop the index with the temperature since the perturbation of the temperature is small compared with the background value. Equation (13) shows that the continuum intensity is also linearised around the background intensity I_0 and that the intensity perturbation is proportional to the density perturbation ρ'. Using the above equations we can calculate the velocity, the magnetic field and the intensity perturbations for different wave modes. From now on we will only work with the perturbed quantities and for notational convenience we will drop the prime.

We will first study the intensity perturbation. We know that the density perturbation ρ is given by $\rho_\mathrm{p} = \rho_0 R(r)\cos(\omega t - kz)\cos(m\varphi)$ in the case of a propagating mode, and by $\rho_\mathrm{st} = \rho_0 R(r)\cos(\omega t)\sin(kz)\cos(m\varphi)$ in the case of a standing mode. This means that the intensity perturbation is given by

$$I_\mathrm{p} = \frac{2}{3}\frac{h\nu}{k_\mathrm{B}T} I_0 R(r)\cos(\omega t - kz)\cos(m\varphi) \tag{14}$$

in the case of a propagating mode, and by

$$I_\mathrm{st} = \frac{2}{3}\frac{h\nu}{k_\mathrm{B}T} I_0 R(r)\cos(\omega t)\sin(kz)\cos(m\varphi) \tag{15}$$

in the case of a standing mode. Fujimura & Tsuneta (2009) studied oscillating photospheric flux tubes using data obtained by Hinode. They obtained the intensity, the LOS velocity, and the LOS magnetic flux fluctuations by averaging over the entire region of interest. Their region of interest is typically the centre of a flux tube. Thus, in order to use their data we need to integrate our equations over r and φ to reproduce the averaging over the flux tube/pixel.

Previously, we considered two values for m, namely the sausage mode ($m = 0$) and the kink mode ($m = 1$). Higher m-values have not been considered. However, in the following argument we will show that the fluxtube-averaged intensity variations vanish for $m \geq 1$. Integrating the intensity perturbation over the flux tube results in

$$\overline{I_\mathrm{p}} = \frac{2}{3}\frac{h\nu}{k_\mathrm{B}T} I_0 \cos(\omega t - kz)\left(\int_0^\mathrm{R} rR(r)\mathrm{d}r\right)\left(\int_0^{2\pi}\cos(m\varphi)\mathrm{d}\varphi\right)$$

in the case of a propagating mode. For the sausage mode it is not necessary to calculate the integral over r; we only need to verify that this integral is non-zero. If this integral is non-zero, it means that the average intensity perturbation in the sausage mode is non-zero. In Eq. (11) we showed that $R(r)$ is proportional to P' and in Sect. 2.2 we plotted the eigenfunction P'. In the case of a sausage mode, the bottom panel in Fig. 3 shows that for surface modes the eigenfunction is always negative which means that the integral $\int_0^\mathrm{R} rR(r)\mathrm{d}r$ will be non-zero. In the case of the body mode, we see that there is a node in the eigenfunction of P' located at $r = r_0$. Since r_0 is close to the flux tube boundary, the integral $\int_0^\mathrm{R} rR(r)\mathrm{d}r$ will be dominated by the area between 0 and r_0 and thus the integral will also be non-zero. The same argument can be used to show that in the case of the standing sausage mode the fluxtube-averaged intensity perturbation is also non-zero. We would like to note that this argument will remain valid even when density stratification is included because the integral is independent of the z-coordinate.

We can also integrate the intensity perturbation over r and φ in the case of the kink mode. Here the integral over r does not matter because the integral of $\cos(\varphi)$ over an entire period is zero. This means that the average intensity perturbation is equal to zero. This same argument also shows that for higher values of m, the average intensity perturbation is zero since the integral of $\cos(m\varphi)$ over an entire period is zero if m is non-zero. This means that we cannot observe an intensity perturbation for a kink wave in a strictly linear theory. Since the observations in Fujimura & Tsuneta (2009) have an intensity perturbation, we can rule out the kink mode as a possible wave mode to explain the observed oscillations. Note that we could include a second order term in the intensity expansion which would ensure a non-zero contribution when averaging over the flux tube. However, a second order term in the intensity expansion would have a period that is half the period of the wave. The intensity observations in Fujimura & Tsuneta (2009) could also be due to this second order term in the intensity expansion in the case of a kink wave since they mention that some of the observations had two peaks in the power spectrum. However, for now, we will continue working with a purely linear theory to describe the perturbations.

We can now calculate the r- and z-components of the velocity and the magnetic field perturbations for different propagating sausage wave modes. The results are

$$\overline{v_{r,\mathrm{p}}} = -\frac{c_\mathrm{s}^2 + c_\mathrm{A}^2}{\omega}\frac{\omega^2 - k^2c_\mathrm{T}^2}{\omega^2 - k^2c_\mathrm{A}^2}\left(\int_0^\mathrm{R} r\frac{\mathrm{d}R}{\mathrm{d}r}\mathrm{d}r\right)\sin(\omega t - kz) \tag{16}$$

$$\overline{v_{z,\mathrm{p}}} = \frac{c_\mathrm{s}^2}{\omega/k}\left(\int_0^\mathrm{R} rR(r)\mathrm{d}r\right)\cos(\omega t - kz) \tag{17}$$

$$\overline{B_{r,\mathrm{p}}} = \frac{B_0}{\omega/k}\frac{c_\mathrm{s}^2 + c_\mathrm{A}^2}{\omega}\frac{\omega^2 - k^2c_\mathrm{T}^2}{\omega^2 - k^2c_\mathrm{A}^2}\left(\int_0^\mathrm{R} r\frac{\mathrm{d}R}{\mathrm{d}r}\mathrm{d}r\right)\sin(\omega t - kz) \tag{18}$$

$$\overline{B_{z,\mathrm{p}}} = B_0\frac{\omega^2 - k^2c_\mathrm{s}^2}{\omega^2}\left(\int_0^\mathrm{R} rR(r)\mathrm{d}r\right)\cos(\omega t - kz). \tag{19}$$

Note that the integration with respect to r only changes the amplitude of the wave modes. In Sect. 2.3.2 it will become clear that the r-dependence of the amplitudes is neglected since we always look at a ratio between two observables.

We can also calculate the r- and z-components of the velocity and magnetic field perturbations in the case of a standing sausage mode resulting in

$$\overline{v_{r,\mathrm{st}}} = -\frac{c_\mathrm{s}^2 + c_\mathrm{A}^2}{\omega}\frac{\omega^2 - k^2c_\mathrm{T}^2}{\omega^2 - k^2c_\mathrm{A}^2}\left(\int_0^\mathrm{R} r\frac{\mathrm{d}R}{\mathrm{d}r}\mathrm{d}r\right)\sin(\omega t)\sin(kz) \tag{20}$$

$$\overline{v_{z,\mathrm{st}}} = -\frac{c_\mathrm{s}^2}{\omega/k}\left(\int_0^\mathrm{R} rR(r)\mathrm{d}r\right)\sin(\omega t)\cos(kz) \tag{21}$$

$$\overline{B_{r,\mathrm{st}}} = \frac{B_0}{\omega/k}\frac{c_\mathrm{s}^2 + c_\mathrm{A}^2}{\omega}\frac{\omega^2 - k^2c_\mathrm{T}^2}{\omega^2 - k^2c_\mathrm{A}^2}\left(\int_0^\mathrm{R} r\frac{\mathrm{d}R}{\mathrm{d}r}\mathrm{d}r\right)\cos(\omega t)\cos(kz) \tag{22}$$

$$\overline{B_{z,\mathrm{st}}} = B_0\frac{\omega^2 - k^2c_\mathrm{s}^2}{\omega^2}\left(\int_0^\mathrm{R} rR(r)\mathrm{d}r\right)\cos(\omega t)\sin(kz). \tag{23}$$

There is no mention of the variable φ in the above equations since we study only $m = 0$ sausage modes. We have already ruled out the $m \geq 1$ modes on the basis of the vanishing area-averaged intensity perturbations.

We remark that in the above phase relations the time-dependence will remain similar even when density stratification is included, but the amplitudes of the perturbations will be different. We would like to note that the averaging over the flux tube is more involved than described here. To obtain the averaged velocity we would need to integrate the velocity using the intensity as a weight function. This would usually require numerical simulations, so in order to continue an analytical theory we have used a simpler way to average the velocity. By just averaging over the flux tube we have an analytic formula for the velocity perturbation which is also a good first approximation for integrating with the intensity as a weight function.

2.3.1. Phase differences

The next step is to look at all possible sausage wave modes and calculate the phase differences between the LOS velocity, the LOS magnetic field, and the intensity perturbations. We will start with a slow propagating surface mode for which we have shown that the longitudinal component is much larger than the perpendicular component at the flux tube boundary. Since we have integrated our perturbations over the entire flux tube, we also need to look at the components inside the flux tube. We know that the longitudinal component is proportional to P' and that the transverse component is proportional to ξ_r. Figure 3 shows that the eigenfunction ξ_r is very similar to the eigenfunction P' for slow sausage surface modes inside the flux tube. This means that if the mode is longitudinal at the flux-tube boundary, it will also behave longitudinally inside the flux tube. Thus the velocity perturbation is given by Eq. (17), the magnetic field perturbation is given by Eq. (19), and the intensity perturbation is given by Eq. (14). The LOS does not matter in this case since the modes are dominated by the longitudinal component and the LOS contribution is $\cos(\theta)$, which will be added to the amplitudes later. Since the wave is a slow mode, we also know that $\omega^2 - k^2c_\mathrm{s}^2$ is negative (see Fig. 2). Because the LOS velocity, the LOS magnetic field, and the intensity perturbations all vary with $\cos(\omega t - kz)$, it is straightforward to calculate the phase differences. We use ϕ_v as a notation for the phase of the velocity perturbation, ϕ_B as a notation for the phase of the magnetic field perturbation, and ϕ_I as a notation for the phase of the intensity perturbation. We find that $\phi_B - \phi_v = \pi$, $\phi_v - \phi_I = 0$ and $\phi_I - \phi_B = \pi$. These results are listed in Table 1.

The second case is the slow standing surface mode which is also dominated by the longitudinal component. This means that the LOS will again be neglected and later added in the amplitudes. This also means that the velocity perturbation is given by Eq. (21), the magnetic field perturbation is given by Eq. (23), and the intensity perturbation is given by Eq. (15). As with the propagating slow mode, $\omega^2 - k^2c_\mathrm{s}^2$ is again negative. From this information it is possible to calculate the phase differences resulting in

$$\phi_B - \phi_v = \begin{cases} \frac{\pi}{2} & \text{if } 0 \leq kz + n\pi \leq \pi/2 \\ -\frac{\pi}{2} & \text{if } \pi/2 \leq kz + n\pi \leq \pi \end{cases}$$

$$\phi_v - \phi_I = \begin{cases} \frac{\pi}{2} & \text{if } 0 \leq kz + n\pi \leq \pi/2 \\ -\frac{\pi}{2} & \text{if } \pi/2 \leq kz + n\pi \leq \pi \end{cases}$$

$$\phi_I - \phi_B = \pi,$$

where n is an integer and is determined by the height at which we observe the wave. This result can also be seen in Table 1. Figure 6 shows a visualisation of the slow standing sausage surface mode. The left part shows the velocity perturbation, while the right part shows the magnetic field perturbation. The phase shift angle α_z is taken equal to zero. From the visualisation it is possible to deduce the phase difference between the magnetic field and the velocity; note that they match the theoretical values. Using this figure it is also clear that the phase differences are periodic with period π. This figure also confirms that n in the above formulas is determined by the height at which we observe, since the origin of the sytem $kz = 0$ is chosen arbitrarily.

The third case is the fast propagating mode for which we have shown that the transverse and the longitudinal components of the displacement have roughly the same magnitude at the flux-tube boundary. We need to look at the behaviour inside the flux tube as well. Figure 3 shows that for a fast sausage surface mode the eigenfunction P' is larger than the eigenfunction ξ_r inside the flux tube. This means that inside the flux tube the longitudinal component is larger than the transverse component, while at the flux-tube boundary they are roughly equal. Since we have performed a Fourier analysis of all quantities with respect to time, we know that the magnitude of the velocity perturbation is proportional to the magnitude of the displacement, i.e. $\boldsymbol{v} = \partial\boldsymbol{\xi}/\partial t = \mathrm{i}\omega\boldsymbol{\xi}$. Thus, the velocity behaves the same way as the

Table 1. Phase differences between the LOS velocity perturbation, the LOS magnetic field perturbation, and the intensity perturbation for different sausage wave modes.

Wave mode	$\phi_B - \phi_v$	$\phi_v - \phi_I$	$\phi_I - \phi_B$
Slow propagating	π	0	π
Fast propagating surface	$[0, \pi]$	$[-\pi/2, 0]$	$[-\pi/2, 0]$
Slow standing	$\pm\pi/2$	$\pm\pi/2$	π
Fast standing surface	$\pm\pi/2$	$\pm\pi/2$	$0,\pi$

Notes. We use ϕ_v as a notation for the phase of the LOS velocity perturbation, ϕ_B as a notation for the phase of the LOS magnetic field perturbation, and ϕ_I as a notation for the phase of the intensity perturbation. For the fast modes we have assumed the widest possible range for θ, q, $\phi_{B,\mathrm{p}}$, $\phi_{B,\mathrm{st}}$, $\phi_{v,\mathrm{p}}$, and $\phi_{v,\mathrm{st}}$.

displacement, meaning that the magnitude of v_r should roughly be the same as the magnitude of v_z at the flux-tube boundary, while the magnitude of v_r should be smaller than the magnitude of v_z inside the flux tube. We will use $|\overline{v_r}| = q|\overline{v_z}|$ where q is a constant between 0 and 1 to indicate that the transverse component is smaller than the longitudinal component. From observations, we also know the LOS angle θ (i.e. the helio-longitudinal angle from the meridional line, see Fig. 1), and using this angle we can calculate the LOS velocity perturbation and the LOS magnetic field perturbation. We find that

$$\overline{v_{\mathrm{LOS}}} = A_{v,\mathrm{p}} \cos(\omega t - kz - \phi_{v,\mathrm{p}}) \tag{24}$$

$$\overline{B_{\mathrm{LOS}}} = A_{B,\mathrm{p}} \cos\left(\omega t - kz + \phi_{B,\mathrm{p}}\right), \tag{25}$$

where $\phi_{v,\mathrm{p}}$ and $\phi_{B,\mathrm{p}}$ are phase shifts; $A_{v,\mathrm{p}}$ and $A_{B,\mathrm{p}}$ are the amplitudes of the LOS perturbations and are given by

$$A_{v,\mathrm{p}} = \frac{c_\mathrm{s}^2}{\omega/k}\left(\int_0^\mathrm{R} rR(r)\mathrm{d}r\right)\sqrt{q^2\sin(\theta)^2 + \cos(\theta)^2}$$

$$A_{B,\mathrm{p}} = \frac{B_0 c_\mathrm{s}^2}{\omega^2/k^2}\left(\int_0^\mathrm{R} rR(r)\mathrm{d}r\right)\sqrt{q^2\sin^2(\theta) + \left(\frac{\omega^2 - k^2c_\mathrm{s}^2}{k^2c_\mathrm{s}^2}\right)^2\cos^2(\theta)}$$

$$\phi_{v,\mathrm{p}} = \arctan\left(q\tan(\theta)\right)$$

$$\phi_{B,\mathrm{p}} = \arctan\left(q\tan(\theta)\frac{k^2c_\mathrm{s}^2}{\omega^2 - k^2c_\mathrm{s}^2}\right).$$

Note that q depends on kR and equilibrium parameters. We believe that the value q can be used to calculate the internal Alfvén speed $c_{\mathrm{A,i}}$ when kR is known and vice versa. For the moment we will not use q for seismological purposes, but if this behaviour is present in more advanced equilibrium models we will use it to do seismology.

From Eqs. (14), (24), and (25) it is possible to calculate the phase differences between the intensity, the LOS velocity, and the LOS magnetic field perturbations. But first we need to find out how $\phi_{v,\mathrm{p}}$ and $\phi_{B,\mathrm{p}}$ vary with different values of the LOS angle θ, different values for the sound speed, and different values of q. We easily find that $\phi_{v,\mathrm{p}} \in [0, \pi/2]$, since $\theta \in [0, \pi/2]$ and $q \in [0, 1]$. We can also deduce that $\phi_{B,\mathrm{p}} \in [0, \pi/2]$ since $\omega^2 - k^2c_\mathrm{s}^2$ is positive in the case of a fast mode. To find the effect of the sound speed on the phase shift of the LOS magnetic field perturbation, we can fix θ and q for simplicity as $\theta = 45\,^\circ$ and $q = 0.5$. In Fig. 2 we notice that fast modes have phase speeds between

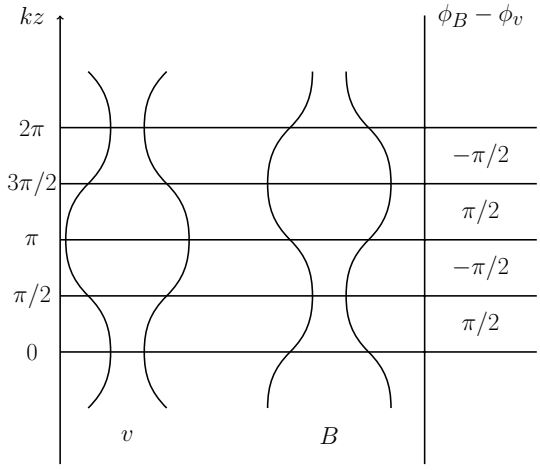

Fig. 6. Phase difference between the magnetic field and the velocity perturbation in the case of a slow standing sausage surface mode. The phase shift α_z is chosen equal to zero.

the internal and the external sound speed, and since the sound speed is directly linked with the temperature we find that

$$0 < \frac{\omega^2 - k^2c_\mathrm{s}^2}{k^2c_\mathrm{s}^2} < \frac{T_\mathrm{e}}{T_\mathrm{i}} - 1. \tag{26}$$

Using the values for temperature found in Fujimura & Tsuneta (2009) we find

$$0 < \frac{\omega^2 - k^2c_\mathrm{s}^2}{k^2c_\mathrm{s}^2} < 0.43.$$

This is a narrow range, and in the case that $\theta = \pi/4$ radians and $q = 0.5$, we find that $\phi_{v,\mathrm{p}} \in [0, \pi/7]$ radians and $\phi_{B,\mathrm{p}} \in [0.87, \pi/2]$ radians. We can now calculate the phase differences between the intensity, the LOS velocity, and the LOS magnetic field perturbations and we find that

$$\phi_B - \phi_v = \phi_{B,\mathrm{p}} + \phi_{v,\mathrm{p}}$$

$$\phi_v - \phi_I = -\phi_{v,\mathrm{p}}$$

$$\phi_I - \phi_B = -\phi_{B,\mathrm{p}}.$$

This result can also be seen in Table 1. Note that the information on the phase differences can also be used to deduce the unknown parameter q since we know the LOS angle θ from observation. We find that

$$q = \frac{\tan(\phi_I - \phi_v)}{\tan(\theta)}. \tag{27}$$

We could also deduce the phase speed ω/k using the phase difference $\phi_I - \phi_B$, the sound speed c_s, and the value q, but we will rely on using the amplitude ratios to derive the phase speed as will be shown in Sect. 2.3.2.

The final case is the fast standing mode for which we have shown that the transverse and the longitudinal component of the displacement have roughly the same magnitude. As before, we will assume that $|\overline{v_r}| = q|\overline{v_z}|$ and using the LOS angle θ, we can calculate the LOS velocity perturbation and the LOS magnetic field perturbation resulting in

$$\overline{v_{\mathrm{LOS}}} = A_{v,\mathrm{st}} \sin(\omega t)\cos(kz + \phi_{v,\mathrm{st}}) \tag{28}$$

$$\overline{B_{\mathrm{LOS}}} = A_{B,\mathrm{st}} \cos(\omega t)\sin(kz - \phi_{B,\mathrm{st}}), \tag{29}$$

where $\phi_{v,\mathrm{st}}$ and $\phi_{B,\mathrm{st}}$ are phase shifts; $A_{v,\mathrm{st}}$ and $A_{B,\mathrm{st}}$ are the amplitudes of the LOS perturbations and are given by

$$A_{v,\mathrm{st}} = -\frac{c_\mathrm{s}^2}{\omega/k}\left(\int_0^\mathrm{R} rR(r)\mathrm{d}r\right)\sqrt{q^2\sin(\theta)^2+\cos(\theta)^2}$$

$$A_{B,\mathrm{st}} = \frac{B_0 c_\mathrm{s}^2}{\omega^2/k^2}\left(\int_0^\mathrm{R} rR(r)\mathrm{d}r\right)\sqrt{q^2\sin^2(\theta)+\left(\frac{\omega^2-k^2c_\mathrm{s}^2}{k^2c_\mathrm{s}^2}\right)^2\cos^2(\theta)}$$

$$\phi_{v,\mathrm{st}} = \arctan\left(q\tan(\theta)\right)$$

$$\phi_{B,\mathrm{st}} = \arctan\left(q\tan(\theta)\frac{k^2c_\mathrm{s}^2}{\omega^2-k^2c_\mathrm{s}^2}\right).$$

Note that the phase shifts $\phi_{v,\mathrm{st}}$ and $\phi_{B,\mathrm{st}}$ are the same expression as in the propagating case, so they range from $[0,\pi/2]$ in the general case. We can now calculate the phase differences between the intensity, the LOS velocity, and the LOS magnetic field perturbations and we find that

$$\phi_B-\phi_v = \begin{cases}\frac{\pi}{2} & \text{if } (kz+n\pi)\in A_1\cap A_2\\ -\frac{\pi}{2} & \text{if } \phi_{B,\mathrm{st}}\le kz+n\pi\le\pi/2-\phi_{v,\mathrm{st}}\end{cases}$$

$$\phi_v-\phi_I = \begin{cases}\frac{\pi}{2} & \text{if } 0\le kz+n\pi\le\pi/2-\phi_{v,\mathrm{st}}\\ -\frac{\pi}{2} & \text{if } \pi/2-\phi_{v,\mathrm{st}}\le kz+n\pi\le\pi\end{cases}$$

$$\phi_I-\phi_B = \begin{cases}\pi & \text{if } 0\le kz+n\pi\le\phi_{B,\mathrm{st}}\\ 0 & \text{if } \phi_{B,\mathrm{st}}\le kz+n\pi\le\pi,\end{cases}$$

where

$$A_1 = [\pi/2-\phi_{v,\mathrm{st}}, 3\pi/2-\phi_{v,\mathrm{st}}]$$
$$A_2 = [\phi_{B,\mathrm{st}}, \pi+\phi_{B,\mathrm{st}}]$$

and n is an integer which is again determined by the height at which we observe the wave. These phase differences are also listed in Table 1. We believe that these phase differences will remain largely unchanged when density stratification is included in the model since the time-dependence of the phase relations is largely independent of the density stratification.

2.3.2. Amplitude ratios

From the phase relations of the LOS velocity perturbation, the LOS magnetic field perturbation, and the intensity perturbation it is possible to deduce more information than only the phase differences. We can also compare the amplitudes of the perturbations for different wave modes. Remember that our equilibrium model is very simple and neglects some important physical effects (e.g. density stratification) which means that these amplitude ratios are only an approximation. Since the goal is to invert these amplitude ratios to find unknown parameters, the results of these inversions are only order of magnitude estimates rather than precise values. For notational convenience we shall denote $\overline{v_\mathrm{LOS}}$ by v because from now on we will only work with fluxtube-averaged perturbations. In the case of slow propagating modes we find that

$$\frac{|B|}{|v|} = \frac{B_0}{c_\mathrm{s}^2}\frac{\left|\omega^2/k^2-c_\mathrm{s}^2\right|}{\omega/k} \tag{30}$$

$$\frac{|v|}{|I|} = \frac{3}{2}\frac{k_\mathrm{B}T}{h\nu}\frac{c_\mathrm{s}^2}{\omega/k}\frac{\cos(\theta)}{I_0} \tag{31}$$

$$\frac{|I|}{|B|} = \frac{2}{3}\frac{h\nu}{k_\mathrm{B}T}\frac{I_0}{B_0}\frac{1}{\cos(\theta)}\frac{\omega^2/k^2}{\left|\omega^2/k^2-c_\mathrm{s}^2\right|}, \tag{32}$$

where the terms $\cos(\theta)$ appear because the LOS velocity and the LOS magnetic field are both directed along the LOS, but the intensity is not changed by the viewing direction. We also notice that integration over the r-direction has no influence because the r-dependence is the same for all perturbations. We can do the same in the case of slow standing waves to find

$$\frac{|B|}{|v|} = \frac{B_0}{c_\mathrm{s}^2}\frac{\left|\omega^2/k^2-c_\mathrm{s}^2\right|}{\omega/k}|\tan(kz)| \tag{33}$$

$$\frac{|v|}{|I|} = \frac{3}{2}\frac{k_\mathrm{B}T}{h\nu}\frac{c_\mathrm{s}^2}{\omega/k}\frac{\cos(\theta)}{I_0|\tan(kz)|} \tag{34}$$

$$\frac{|I|}{|B|} = \frac{2}{3}\frac{h\nu}{k_\mathrm{B}T}\frac{I_0}{B_0}\frac{1}{\cos(\theta)}\frac{\omega^2/k^2}{\left|\omega^2/k^2-c_\mathrm{s}^2\right|}. \tag{35}$$

These amplitude ratios depend on the value kz which contains information on the vertical behaviour of the wave, i.e. k is the vertical wavenumber and z is the relative position in a wavelength. In the case of a fast propagating mode we find that

$$\frac{|B|}{|v|} = \frac{B_0}{\omega/k}\frac{\sqrt{q^2\sin^2(\theta)+\left(\frac{\omega^2-k^2c_\mathrm{s}^2}{k^2c_\mathrm{s}^2}\right)^2\cos^2(\theta)}}{\sqrt{q^2\sin(\theta)^2+\cos(\theta)^2}} \tag{36}$$

$$\frac{|v|}{|I|} = \frac{3}{2}\frac{k_\mathrm{B}T}{h\nu}\frac{\sqrt{q^2\sin(\theta)^2+\cos(\theta)^2}}{I_0}\frac{c_\mathrm{s}^2}{\omega/k} \tag{37}$$

$$\frac{|I|}{|B|} = \frac{2}{3}\frac{h\nu}{k_\mathrm{B}T}\frac{I_0}{B_0}\frac{\omega^2/k^2}{c_\mathrm{s}^2}\frac{1}{\sqrt{q^2\sin^2(\theta)+\left(\frac{\omega^2-k^2c_\mathrm{s}^2}{k^2c_\mathrm{s}^2}\right)^2\cos^2(\theta)}}. \tag{38}$$

And finally in the case of fast standing mode we find that

$$\frac{|B|}{|v|} = \frac{B_0}{\omega/k}\left|\frac{\sin(kz-\phi_{B,\mathrm{st}})}{\cos(kz+\phi_{v,\mathrm{st}})}\right|\frac{\sqrt{q^2\sin^2(\theta)+\left(\frac{\omega^2-k^2c_\mathrm{s}^2}{k^2c_\mathrm{s}^2}\right)^2\cos^2(\theta)}}{\sqrt{q^2\sin(\theta)^2+\cos(\theta)^2}} \tag{39}$$

$$\frac{|v|}{|I|} = \frac{3}{2}\frac{k_\mathrm{B}T}{h\nu}\frac{1}{I_0}\frac{c_\mathrm{s}^2}{\omega/k}\left|\frac{\cos(kz+\phi_{v,\mathrm{st}})}{\sin(kz)}\right|\sqrt{q^2\sin(\theta)^2+\cos(\theta)^2} \tag{40}$$

$$\frac{|I|}{|B|} = \frac{2}{3}\frac{h\nu}{k_\mathrm{B}T}\frac{I_0}{B_0}\frac{\omega^2/k^2}{c_\mathrm{s}^2}\frac{\left|\frac{\sin(kz)}{\sin(kz-\phi_{B,\mathrm{st}})}\right|}{\sqrt{q^2\sin^2(\theta)+\left(\frac{\omega^2-k^2c_\mathrm{s}^2}{k^2c_\mathrm{s}^2}\right)^2\cos^2(\theta)}}. \tag{41}$$

The amplitude ratios are not useful in this notation since we want to use the amplitude ratios to find information on the phase speed, for example. This means that we need to invert these ratios. We will start with the slow propagating mode from which it is possible to find an estimate for the phase speed and the sound speed using an estimate for the temperature. Using Eq. (31) we find that

$$\frac{\omega}{k} = \frac{3}{2}\frac{k_\mathrm{B}}{h\nu}\cos(\theta)\frac{|I|/I_0}{|v|/c_\mathrm{s}}\sqrt{\frac{\gamma k_\mathrm{B}}{\bar{\mu}m_\mathrm{p}}}T^{3/2} = \sqrt{A_{\mathrm{s,p}}}T^{3/2},$$

where we have used

$$c_\mathrm{s} = \sqrt{\frac{\gamma k_\mathrm{B}T}{\bar{\mu}m_\mathrm{p}}}. \tag{42}$$

In this equation we introduced the average molecular weight $\bar{\mu}$ and the mass of a proton m_p. Using Eq. (32) and the fact that $|\omega^2/k^2 - c_\mathrm{s}^2| = c_\mathrm{s}^2 - \omega^2/k^2$ (we are dealing with a slow mode), we find

$$\frac{\gamma k_\mathrm{B} T}{\bar{\mu} m_\mathrm{p}} \frac{|I|/I_0}{|B|/B_0} - A_\mathrm{s,p} \frac{|I|/I_0}{|B|/B_0} T^3 = \frac{2}{3} \frac{h\nu}{k_\mathrm{B}} \frac{A_\mathrm{s,p}}{\cos(\theta)} T^2.$$

Rewriting this equation leads to

$$-a_3 T^3 - a_2 T^2 + a_1 T = 0,$$

where a_1, a_2, and a_3 are all positive and are given by

$$a_3 = \left(\frac{3}{2}\frac{k_\mathrm{B}}{h\nu}\right)^2 \cos^2(\theta) \frac{\gamma k_\mathrm{B}}{\bar{\mu} m_\mathrm{p}} \frac{(|I|/I_0)^3}{|B|/B_0\,(|v|/c_\mathrm{s})^2}$$

$$a_2 = \frac{3}{2}\frac{k_\mathrm{B}}{h\nu} \cos(\theta) \frac{\gamma k_\mathrm{B}}{\bar{\mu} m_\mathrm{p}} \left(\frac{|I|/I_0}{|v|/c_\mathrm{s}}\right)^2$$

$$a_1 = \frac{\gamma k_\mathrm{B}}{\bar{\mu} m_\mathrm{p}} \frac{|I|/I_0}{|B|/B_0}.$$

Since the temperature should be strictly positive, we find that an estimate for the temperature is given by

$$T = \frac{a_2 - \sqrt{a_2^2 + 4 a_3 a_1}}{-2 a_3}, \tag{43}$$

where we discarded the solution with the + sign because that would lead to a negative temperature. Note that all the amplitude ratios are now written in dimensionless form.

The next amplitude ratios to invert are the ones describing a slow standing mode. From these it is possible to find an estimate for the phase speed and the value $|\tan(kz)|$. We solve Eq. (35) for ω/k using $|\omega^2/k^2 - c_\mathrm{s}^2| = c_\mathrm{s}^2 - \omega^2/k^2$ (we are dealing with a slow mode) to find

$$\frac{\omega}{k} = c_\mathrm{s} \sqrt{\frac{|I|/I_0}{|B|/B_0}} \left[\frac{2}{3}\frac{h\nu}{k_\mathrm{B} T}\frac{1}{\cos(\theta)} + \frac{|I|/I_0}{|B|/B_0}\right]^{-1/2}. \tag{44}$$

To calculate the value $|\tan(kz)|$, we use Eq. (34) to find

$$|\tan(kz)| = \frac{3}{2}\frac{k_\mathrm{B} T}{h\nu}\frac{c_\mathrm{s}}{\omega/k}\frac{|I|/I_0}{|v|/c_\mathrm{s}}\cos(\theta). \tag{45}$$

The amplitude ratios for fast propagating modes can be inverted to find an estimate for the phase speed and the sound speed. Using Eq. (37) we find

$$\frac{\omega}{k} = \frac{3}{2}\frac{k_\mathrm{B}}{h\nu}\frac{\bar{\mu} m_\mathrm{p}}{\gamma k_\mathrm{B}} \sqrt{q^2 \sin(\theta)^2 + \cos(\theta)^2} \frac{|I|/I_0}{|v|/c_\mathrm{s}} (c_\mathrm{s})^3 = A_\mathrm{f,p} (c_\mathrm{s})^3. \tag{46}$$

Using this combined with Eq. (36) we find an equation which can be solved numerically to estimate the sound speed c_s, namely

$$A_\mathrm{f,p} c_\mathrm{s}^2 \frac{|B|/B_0}{|v|/c_\mathrm{s}} = \frac{\sqrt{q^2 \sin^2(\theta) + \left(A_\mathrm{f,p} c_\mathrm{s} - 1\right)^2 \cos^2(\theta)}}{\sqrt{q^2 \sin(\theta)^2 + \cos(\theta)^2}}. \tag{47}$$

Finally we have to invert the amplitude ratios for a fast standing mode to find an estimate for the phase speed and the value $\tan(kz)$. Using Eq. (40) we find that

$$\tan(kz) = \frac{\cos(\phi_{v,\mathrm{st}})}{\sin(\phi_{v,\mathrm{st}}) \pm A_\mathrm{f,st}}, \tag{48}$$

where $A_\mathrm{f,st}$ is given by

$$A_\mathrm{f,st} = \frac{2}{3}\frac{h\nu}{k_\mathrm{B} T}\frac{\omega/k}{c_\mathrm{s}}\frac{|v|/c_\mathrm{s}}{|I|/I_0}\frac{1}{\sqrt{q^2 \sin(\theta)^2 + \cos(\theta)^2}}.$$

Using this combined with Eq. (41) we find an equation for the phase speed

$$\left|\cos(\phi_{B,\mathrm{st}}) - \frac{\sin(\phi_{B,\mathrm{st}})}{\tan(kz)}\right| \frac{|I|/I_0}{|B|/B_0} = \frac{\frac{3}{2}\frac{k_\mathrm{B} T}{h\nu}\frac{\omega^2/k^2}{c_\mathrm{s}^2}}{\sqrt{q^2 \sin^2(\theta) + \left(\frac{\omega^2 - k^2 c_\mathrm{s}^2}{k^2 c_\mathrm{s}^2}\right)^2 \cos^2(\theta)}}. \tag{49}$$

This equation needs to be solved numerically since both $\tan(kz)$ and $\phi_{B,\mathrm{st}}$ depend on the phase speed. The information contained in $\tan(kz)$ for both slow and fast standing modes is not very useful because of the possible phase shift in the z-direction α_z. We neglected this phase shift since it only arbitrarily redefines the value $z = 0$. If we add the phase shift again, we are actually computing information on $\tan(kz + \alpha_z)$ which now has two unknowns (z and α_z) with only one equation. As stated earlier, these inversions can only be used to obtain an order of magnitude estimate for the unknown quantities such as the vertical wavenumber. The obtained values are likely to change when additional equilibrium parameters are introduced, such as stratification or flux-tube expansion.

3. Results

In Sect. 2 we have created a mathematical framework for photospheric seismology. We have derived the phase relations of observable quantities, such as the LOS velocity perturbation, the LOS magnetic field perturbation, and the intensity perturbation for different wave modes. Now we can create artificial observations to check the validity of the mathematical framework. This artificial data can be either fast/slow or propagating/standing sausage modes. A Fourier analysis will then be performed to find the power spectrum and the phase differences between the dominant peak in the power spectrum. By comparing the observed phase differences with the theoretical values listed in Table 1 we will determine which mode has been used in the artificial data. Once we have identified the mode, we use the inverted amplitude ratios to find parameters which are not directly observable such as the vertical wave number k. Since the artificial data is based on our analytical model, the seismological results ought to be very close to the actual values used in the data. In Sect. 2.3.2 we have shown that we can find order of magnitude estimates for the sound and phase speeds for propagating modes. For standing modes we can find order of magnitude estimates for the phase speed and the value $\tan(kz)$. By using the power spectrum we can determine the period of the wave, and combining this with the phase speed yields an order of magnitude estimate for the vertical wave number.

All the simulations used the same plasma parameters, namely the ones we used in the dispersion diagram (Fig. 2). This means that we took $c_\mathrm{A,i} = 2\,c_\mathrm{s,i}$, $c_\mathrm{A,e} = 0.5\,c_\mathrm{s,i}$, and $c_\mathrm{s,e} = 1.5\,c_\mathrm{s,i}$, and in doing so we normalised all the velocities using the internal sound speed. We took $kR = 1.0$ using a normalisation in terms of k. We also fixed z for all the simulations and have chosen $kz = 0.5$. We also used values from Fujimura & Tsuneta (2009) for the frequency of the electromagnetic wave ν and the average molecular weight in the photosphere $\bar{\mu}$. To further compare with the data in Fujimura & Tsuneta (2009), we simulated the same

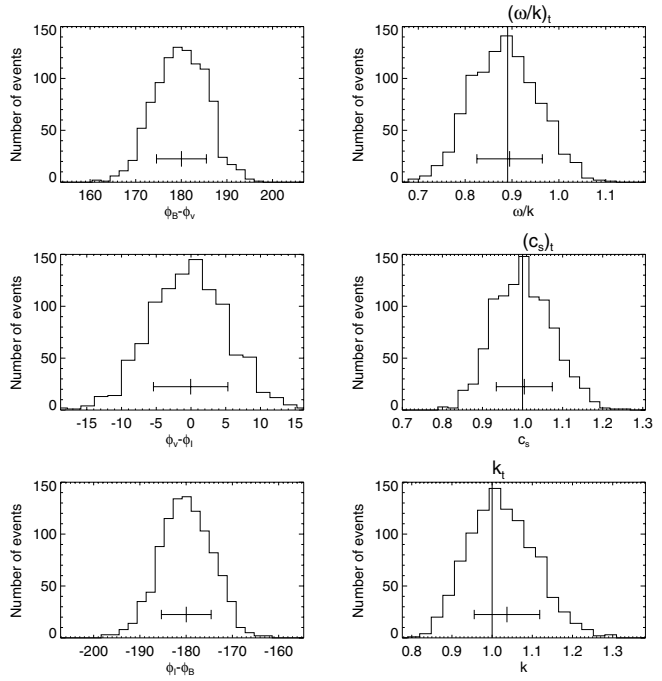

Fig. 7. Results of the Fourier analysis on artificial data obtained by simulating a slow propagating wave mode. The left histograms show the phase differences between perturbations in the LOS magnetic field, the LOS velocity, and the intensity. The right histograms show the phase speed ω/k, the sound speed c_s, and the vertical wave number k which have been calculated from the inverted amplitude ratios. The average of the histograms is indicated by the short vertical line and one standard deviation by the horizontal line. In the right histograms there is also a vertical line showing the value used in the simulation.

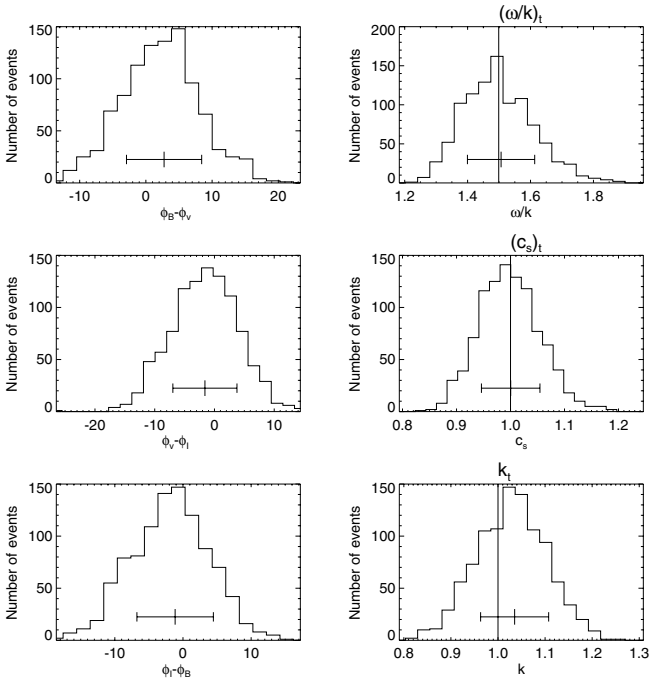

Fig. 8. Results of the Fourier analysis on artificial data obtained by simulating a fast propagating wave mode. The left histograms show the phase differences between perturbations in the LOS magnetic field, the LOS velocity, and the intensity. The right histograms show the phase speed ω/k, the sound speed c_s, and the vertical wave number k which have been calculated from the inverted amplitude ratios assuming $q = 0.04$.

number of periods as they observed, using the same cadence. This is roughly equal to 12.5 periods and about 4 to 5 datapoints per period. We used a LOS angle θ of 30 degrees since this is also comparable to the observations in Fujimura & Tsuneta (2009). We added Gaussian-distributed noise to the artificial data, and we put an arbitrary standard deviation σ of 100 percent of the perturbation.

The first case is a slow propagating mode (Fig. 7). The left side shows the phase differences between the perturbations in the LOS magnetic field, the LOS velocity, and the intensity. These show concentrations around 180° for $\phi_B - \phi_v$, around 0° for $\phi_v - \phi_I$, and around −180° for $\phi_I - \phi_B$. If we compare these observed values with the theoretical values in Table 1, we conclude that this can only be a slow propagating mode and our analysis thus confirms what we have simulated. The next step is to use the amplitude ratios between perturbations in the LOS magnetic field, the LOS velocity, and the intensity to estimate the phase speed ω/k and the sound speed c_s. The results of those estimates can be seen in the histograms on the right side in Fig. 7. In the histograms the average is indicated by the short vertical line; the standard deviation is plotted using a horizontal line. In some of the histograms there is a long vertical line indicating the value used in the simulation. We can clearly see that the average is near the theoretical value in each of the histograms and the theoretical value is certainly contained within one standard deviation. This means that our algorithm works correctly for a slow propagating mode even when noise is included. The algorithm is robust until the LOS angle θ becomes too large, in this case larger than 89 degrees (but angles this high are not observable). For large angles the LOS observation is actually just the transverse component which we neglected in the case of slow modes. The algorithm also works for larger values of kR with similar precision.

The next simulation is a fast propagating mode (Fig. 8). On the left side in Fig. 8 we again have the histograms that show the phase differences and upon comparison with the theoretical values in Table 1 we can conclude that the only possible mode is a fast propagating mode. In Sect. 2.3.1 we showed that the parameter q will be lower than 1 since the longitudinal component is larger than the transverse component inside the flux tube. Equation (27) shows how to calculate this parameter q, and in this case we find $q = 0.04$ which means that the observation is almost completely dominated by the longitudinal component. In the histograms on the right side we show the estimated values of the phase speed ω/k, the sound speed c_s, and the vertical wave number k. As before, the estimated value and the actual value in the simulation match within one standard deviation. As before, the algorithm has no problems with higher values of the LOS angle θ and no problems with higher values of kR.

The next simulation is a slow standing mode, the results of which are shown in Fig. 9. On the left side we have histograms showing the phase differences, but upon comparison with the theoretical values in Table 1 we conclude that both the slow standing mode or the fast standing mode are candidates. On the right we show histograms with the estimated phase speed ω/k, the vertical wave number k, and the value $|\tan(kz)|$ under the assumption that we are dealing with a standing slow mode. We can see that the phase speed ω/k and the value $|\tan(kz)|$ match the value used in the artificial data very closely. The vertical wave number k is slightly overestimated. Since the data is discrete, the Fourier analysis results in discrete values for the period of the wave. We noticed that the period with which we simulate the wave is located directly between two of the discrete values in the

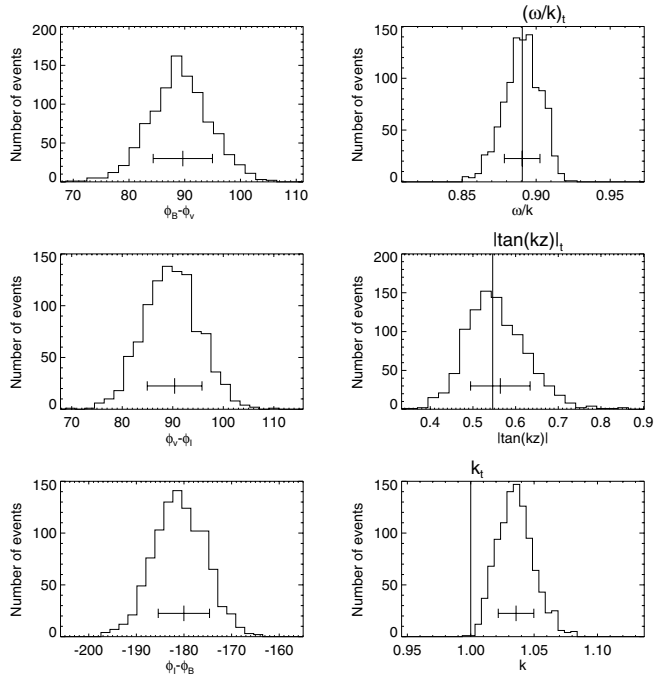

Fig. 9. Results of the Fourier analysis on artificial data obtained by simulating a slow standing wave mode. The left histograms show the phase differences between perturbations in the LOS magnetic field, the LOS velocity, and the intensity. The right histograms show the phase speed ω/k, the value $|\tan(kz)|$, and the vertical wave number k which have been calculated from the inverted amplitude ratios.

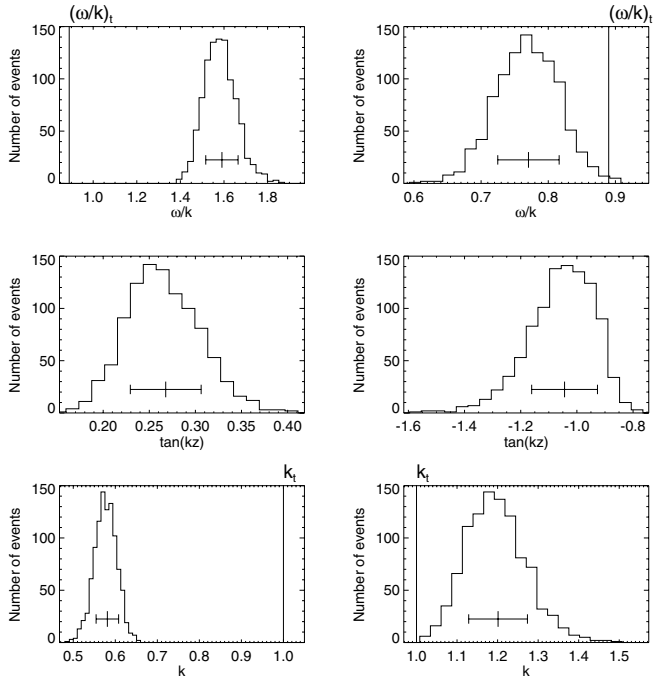

Fig. 10. Results of the Fourier analysis on artificial data obtained by simulating a slow standing wave mode which is interpreted as a fast standing mode. We use the value $q = 1$. The left panel shows the phase speed ω/k, the value $\tan(kz)$, and the vertical wave number k calculated using Eqs. (48) and (49). The *right panel* is a different solution of Eqs. (48) and (49) and shows the phase speed ω/k, the value $\tan(kz)$, and the vertical wave number k. In some histograms there is also a vertical line to indicate the value used in the simulations, and it is clearly visible that this value does not match the results.

Fourier analysis resulting in a slight mismatch. The overestimate is only four percent which is still a very small error. As before, this technique works for different values of kR and for different values of θ provided that the pore is on the disk.

We come back to the issue of the mode ambiguity. Could the wave be wrongly interpreted as a fast standing mode? Figure 10 shows the result when we assume that this observation is a fast standing mode with $q = 1$. Note that Eq. (49) has, in general, four solutions because of the modulus and the ± sign. We only plotted two solutions for the phase speed instead of four, but this is done because the other values for the phase speed were values that exceeded the external sound speed or were lower than the internal sound speed, and so physically impossible (we can determine the sound speed using the temperature). The average of the histograms is far from the value in the simulation, but we cannot rule out these results on the basis of unphysical phase speeds or unphysical vertical wave numbers. Of course we can change the parameter q, but we have no way of calculating this parameter from the phase differences for a fast standing mode. We will use $q = 0.05$ based on the simulation with the fast propagating mode. The result is shown in Fig. 11. We note that the average is still far away from the actual value in the simulation, but the spread of the histograms has decreased. This was to be expected since the standing slow mode is a longitudinal mode and using $q = 0.05$ mimics this longitudinal behaviour. This shows that our mathematical framework is not perfect, as it can not distinguish between some wave modes.

The final simulation is a fast standing mode (Fig. 12). On the left side we have histograms showing the phase differences, and upon comparison with the theoretical values in Table 1 we conclude that this must be a fast standing mode. On the right we show histograms showing the phase speed, the vertical wave number, and the value $\tan(kz)$ estimated under the assumption $q = 1$. We still notice that both the phase speed and the vertical wave number are quite far from the theoretical values. This is again because we assumed that the transverse and longitudinal components of the velocity are equal, while this is not the case for a fast sausage mode when $kR \sim 1$. For this mode there is no easy way to calculate q using the phase differences. Therefore, we have used an arbitrary $q = 0.05$ based on the simulation of the fast propagating mode. The results (Fig. 13) are clearly much better with this value of q, showing again that the longitudinal component is more important than the transverse component. Note that in this simulation we can distinguish the wave modes based on the predicted phase difference, while in the simulation of the slow standing mode there was no distinction between slow or fast standing modes. Table 1 shows that the predicted phase differences of slow and fast standing modes only differ in $\phi_I - \phi_B$ where there are more possibilities for fast standing modes. Thus, simulating a slow standing mode can always be interpreted as either slow or fast, but not necessarily the other way around.

After testing the method on artificial data, we applied our model to the observations in Fujimura & Tsuneta (2009). They interpreted the observations as either slow standing sausage modes or fast standing kink modes. With our improved model, we exclude the second interpretation, but add another possibility: fast standing sausage mode. Even with our improved model, we cannot uniquely identify the observed mode. Using our new inversion technique, we find $kR \approx 5$, strengthening the results of Fujimura & Tsuneta (2009) by obtaining it again with an improved model. Of course, these inferred short wavelengths lead us to believe that even our improved model is not realistic enough to explain the oscillations in all their detail. Further

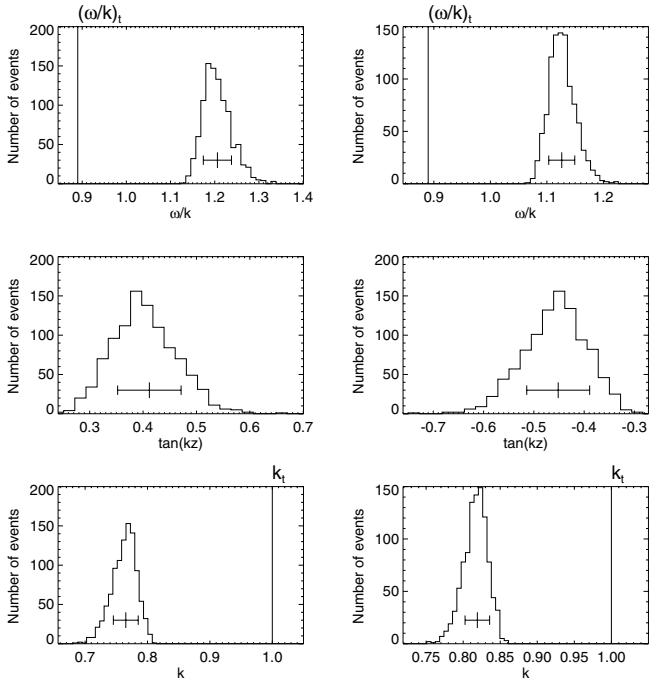

Fig. 11. Results of the Fourier analysis on artificial data obtained by simulating a slow standing wave mode which is interpreted as a fast standing mode. We use the value $q = 0.05$. The *left panel* shows the phase speed ω/k, the value $\tan(kz)$, and the vertical wave number k calculated using Eqs. (48) and (49). The *right panel* is a different solution of Eqs. (48) and (49) and shows the phase speed ω/k, the value $\tan(kz)$, and the vertical wave number k. In some histograms there is also a vertical line to indicate the value used in the simulations, and it is clearly visible that this value does not match the results.

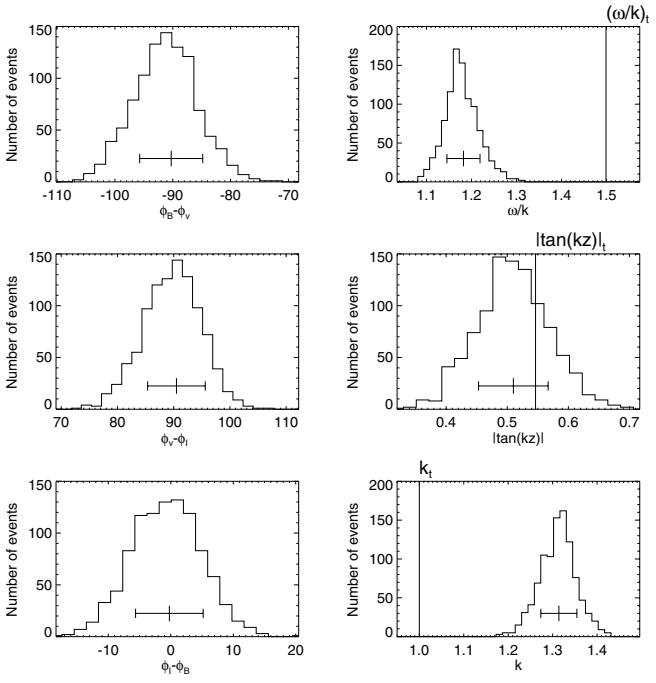

Fig. 12. Results of the Fourier analysis on artificial data obtained by simulating a fast standing wave mode. The left histograms show the phase differences between perturbations in the LOS magnetic field, the LOS velocity, and the intensity. The right histograms show the phase speed ω/k, the value $\tan(kz)$, and the vertical wave number k which have been calculated from the inverted amplitude ratios assuming $q = 1$.

investigation in including flux-tube expansion or density stratification into the model is necessary in the future.

4. Conclusions

We have shown that waves in photospheric flux tubes can be used to find order of magnitudes estimate for parameters that are not directly observable below the visible surface, i.e. to perform photospheric seismology. We have done this by modelling the flux tube as a straight cylinder with constant radius and constant plasma parameters both inside and outside the flux tube. Our model is an improvement upon the modelling done in Fujimura & Tsuneta (2009) because it includes a non-zero gas pressure in the equilibrium model, it does not use the thin tube approximation, and because we used an underdense pore rather than an overdense pore. This model omits some important physical effects (e.g. density stratification) in the equilibrium model. Using the linearised MHD equations, we calculated the dispersion relation for different wave modes in the photosphere. We numerically solved the dispersion relations to find the phase speed of the different wave modes. We studied the wave polarisations by calculating the displacement of the plasma at the flux tube boundary and comparing the longitudinal and transverse components. Using the wave polarisations, we derived phase relations for different observable quantities for both propagating and standing wave modes. Observations are usually integrated over the pore and we showed that first order fluxtube-averaged intensity variations are zero when m is non-zero. Since observations do show intensity variations, we decided to study only sausage modes ($m = 0$). After having calculated the phase relations, we derived the phase differences and the amplitude ratios between the different observable quantities.

The uniform straight cylinder is a simple model but improves upon the previous modelling done in Fujimura & Tsuneta (2009), although it still neglects some important physical effects (e.g. density stratification) which will be adressed in the future modelling. Our improved method obtains $kR \approx 5$ which had previously been found by Fujimura & Tsuneta (2009). While the estimated values for kR are certainly high, they are not necessarily unreasonable. In their review paper, Kosovichev (2012) mentions different sunspot models. In one of the models, sunspots and pores are in fact shallow structures which penetrate less than 2 Mm into the solar interior. The observed radius of the pore studied by Fujimura & Tsuneta (2009) is also of the order of 2 Mm. A standing wave in such a structure would have kR larger than 1. We do not claim that our seismological estimates are proof that the shallow sunspot model is applicable here. We merely want to point out that the obtained wave properties could be compatible with previously developed models for pore or sunspot structures.

We used artificial data to test the validity of our mathematical framework. These tests have shown that the phase differences between the different observables can be used to distinguish between different wave modes and mostly do correct wave mode identification. The tests have also shown that a correct wave mode identification leads to the correct plasma parameters when inverting the amplitude ratios, even when the noise level is 100%. In the case of slow modes we have found no algorithmic limitations on the LOS angle θ and the value kR. The fast modes have proven more challenging for the mathematical framework since the inverted amplitude ratios usually give rise to spurious solutions for the phase speed. However, we have shown that it is possible to discard some of these spurious solutions and that

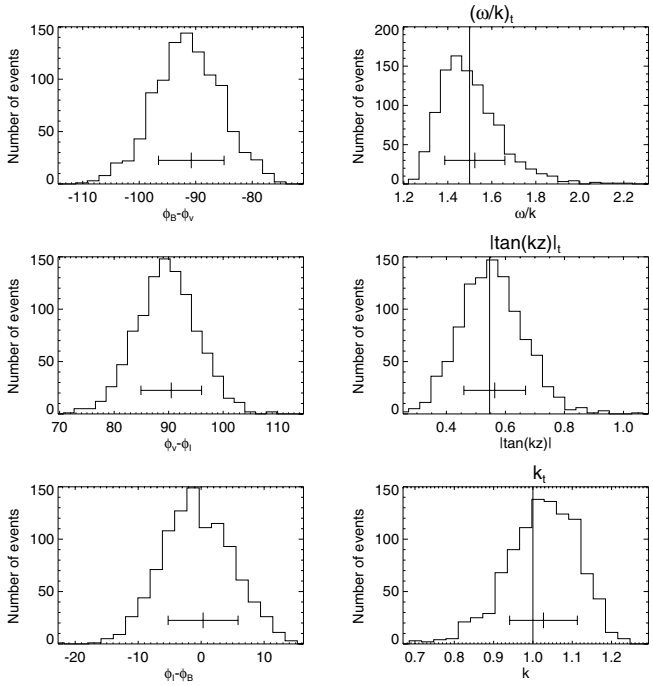

Fig. 13. Results of the Fourier analysis on artificial data obtained by simulating a fast standing wave mode. The left histograms show the phase differences between perturbations in the LOS magnetic field, the LOS velocity, and the intensity. The right histograms show the phase speed ω/k, the value $\tan(kz)$, and the vertical wave number k which were calculated from the inverted amplitude ratios assuming $q = 0.05$.

the inversion of the amplitude ratios also provides the correct plasma parameters.

We have presented a mathematical framework for seismology of photospheric flux tubes using a uniform straight cylinder as a flux tube model. Different wave modes in the photosphere have been described by the linearised ideal MHD equations. The wave mode polarisations allowed us to calculate phase relations, which in turn led to phase differences and amplitude ratios between different observable quantities. This framework has been tested using artificial observations and has also been applied to observations to find order of magnitude estimates for the vertical wavenumber k.

Acknowledgements. We have received funding from the Odysseus programme of the FWO-Vlaanderen and from the EU's Framework Programme 7 as an ERG with grant number 276808.

References

Andries, J., Goossens, M., Hollweg, J. V., Arregui, I., & Van Doorsselaere, T. 2005, A&A, 430, 1109
Aschwanden, M. J., Nightingale, R. W., Andries, J., Goossens, M., & Van Doorsselaere, T. 2003, ApJ, 598, 1375
Banerjee, D., Pérez-Suárez, D., & Doyle, J. G. 2009, A&A, 501, L15
De Pontieu, B., McIntosh, S. W., Carlsson, M., et al. 2007, Science, 318, 1574
Deubner, F.-L. 1983, Sol. Phys., 82, 103
Edwin, P. M., & Roberts, B. 1983, Sol. Phys., 88, 179
Erdélyi, R., Malins, C., Tóth, G., & de Pontieu, B. 2007, A&A, 467, 1299
Fujimura, D., & Tsuneta, S. 2009, ApJ, 702, 1443
Gizon, L., & Birch, A. C. 2005, Liv. Rev. Solar Phys., 2, 6
Goossens, M., Arregui, I., Ballester, J. L., & Wang, T. J. 2008, A&A, 484, 851
Goossens, M., Andries, J., Soler, R., et al. 2012, ApJ, 753, 111
Jess, D. B., Mathioudakis, M., Erdélyi, R., et al. 2009, Science, 323, 1582
Jess, D. B., Pascoe, D. J., Christian, D. J., et al. 2012a, ApJ, 744, L5
Jess, D. B., Shelyag, S., Mathioudakis, M., et al. 2012b, ApJ, 746, 183
Kosovichev, A. G. 2012, Sol. Phys., 134
Leighton, R. B. 1960, in Aerodynamic Phenomena in Stellar Atmospheres, ed. R. N. Thomas, IAU Symp., 12, 321
Liu, W., Nitta, N. V., Schrijver, C. J., Title, A. M., & Tarbell, T. D. 2010, ApJ, 723, L53
Morton, R. J., Erdélyi, R., Jess, D. B., & Mathioudakis, M. 2011, ApJ, 729, L18
Morton, R. J., Verth, G., McLaughlin, J. A., & Erdélyi, R. 2012, ApJ, 744, 5
Nakariakov, V. M., & Verwichte, E. 2005, Liv. Rev. Solar Phys., 2, 3
Nakariakov, V. M., Ofman, L., Deluca, E. E., Roberts, B., & Davila, J. M. 1999, Science, 285, 862
Osterbrock, D. E. 1961, ApJ, 134, 347
Rosenthal, C. S., Bogdan, T. J., Carlsson, M., et al. 2002, ApJ, 564, 508
Rutten, R. J. 2003, Radiative Transfer in Stellar Atmospheres, ed. R. J. Rutten
Sakurai, T., Goossens, M., & Hollweg, J. V. 1991, Sol. Phys., 133, 227
Stein, R. F., & Leibacher, J. 1974, ARA&A, 12, 407
Thompson, B. J., Gurman, J. B., Neupert, W. M., et al. 1999, ApJ, 517, L151
Tomczyk, S., McIntosh, S. W., Keil, S. L., et al. 2007, Science, 317, 1192
Uchida, Y. 1970, PASJ, 22, 341
Ulrich, R. K. 1970, ApJ, 162, 993
Van Doorsselaere, T., Nakariakov, V. M., & Verwichte, E. 2008, ApJ, 676, L73
Van Doorsselaere, T., De Groof, A., Zender, J., Berghmans, D., & Goossens, M. 2011a, ApJ, 740, 90
Van Doorsselaere, T., Wardle, N., Del Zanna, G., et al. 2011b, ApJ, 727, L32